

Multidimensional imaging reveals mechanisms controlling label-free biosensing in vertical 2DM-heterostructures

Tetyana Ignatova^{‡*}, Sajedeh Pourianejad[‡], Xinyi Li[†], Kirby Schmidt[‡],
Frederick Aryeetey[∨], Shyam Aravamudhan[∨], Slava V. Rotkin^{†**}
[‡]*Department of Nanoscience, University of North Carolina at Greensboro,
2907 East Gate City Blvd, Greensboro, North Carolina 27401,
USA;* [†]*Department of Engineering Science and Mechanics,
The Pennsylvania State University, University Park,
Pennsylvania 16802, USA;* [∨]*Department of Nanoengineering,
North Carolina A&T State University, 2907 East Gate City Blvd,
Greensboro, NC 27401, USA;* ^{*}*Materials Research Institute,
The Pennsylvania State University, Millennium Science Complex,
University Park, Pennsylvania 16802, USA;* ^{*} *corresponding authors.*

Two-dimensional materials and their van der Waals heterostructures enable a large range of applications, including label-free biosensing. Lattice mismatch and work function difference in the heterostructure material result in strain and charge transfer, often varying at nanometer scale, that influence device performance. In this work, a multidimensional optical imaging technique is developed in order to map sub-diffractive distributions for doping and strain and understand the role of those for modulation of electronic properties of the material. As an example, vertical heterostructure comprised of monolayer graphene and single layer flakes of transition metal dichalcogenide MoS₂ is fabricated and used for biosensing. Herein, an optical label-free detection of doxorubicin, a common cancer drug, is reported via three independent optical detection channels (photoluminescence shift, Raman shift and Graphene Enhanced Raman Scattering). Non-uniform broadening of components of multimodal signal correlates with the statistical distribution of local optical properties of the heterostructure. Multidimensional nanoscale imaging allows one to reveal the physical origin for such a local response and propose the best strategy for mitigation of materials variability and future device fabrication.

TABLE I. The PL fit parameters for Fig.1(d): upper/lower row corresponds to PL with/without DOX

Trion			A-exciton			B-exciton		
ω_c , eV	γ , meV	P, cts.	ω_c , eV	γ , meV	P, cts.	ω_c , eV	γ , meV	P, cts.
1.739 ± 0.002	$60. \pm 3.$	32 ± 4	1.815 ± 0.0002	82.0 ± 0.3	793 ± 4	1.953 ± 0.001	$135.8 \pm 2.$	203 ± 1
1.719 ± 0.003	$60. \pm 9.$	15 ± 3	1.806 ± 0.002	90.7 ± 0.3	586 ± 3	1.955 ± 0.002	$135.0 \pm 2.$	197 ± 2

I. INTRODUCTION

Emergent need to achieve better, more precise and sensitive drug detection in medicine and health care recently has been addressed by developing biosensors based on two-dimensional materials (2DM)¹⁻⁸. Not only 2D materials offer new response and/or transduction mechanisms and better performance, they can be used for label-free biosensing. Importantly, 2DMs could be designed and/or integrated to generate several signals in response to a single analyte, as it will be illustrated below, or to respond by several channels to a group of substances in parallel, thus achieving a multimodal detection.

The multimodal operation exceeds single-mode biosensing through its higher throughput as well as ability to differentiate the analyte from background signals in a complex media, and potentially allows the multiplexing of biosensing⁹⁻¹³, *i.e.*, determining multiple analytes through a single test. While significant attention has been paid to exploring new 2D materials and demonstrating their biosensing capabilities at the level of single devices¹⁴⁻¹⁷, overall knowledge on what allows successful multimodal detection and what limits biosensing capabilities of 2DM heterostructures is scarce. Atomically thin 2D materials, having an ultimate surface-to-volume ratio, may possess surface non-uniformities at the nanometer scale (atomic impurities/adsorbates/defects, wrinkles/ruptures) that modulate their optical properties, although their importance and explicit role in producing material's variability yet to be studied. To a large extent, the difficulty to determine physical mechanisms that control performance of 2DM devices is due to disparate scales for atomic non-uniformities compared to a micrometer, or larger, size of active elements of a biosensor. Structural characterization with a high spatial resolution, such as electron microscopy, often does not detect materials optical properties, while optical microscopy lacks the required resolution. Thus, in order to reveal such mechanisms, multiple characterization tools should be combined and correlated¹⁸. In this work, correlated multidimensional imaging, including Raman and near-field microscopies, scanning probe and electron microscopies, was applied to unveil physical processes behind label-free multimodal detection of doxorubicin (DOX), an anthracycline cancer drug, by 2DM vertical heterostructures.

Doxorubicin is one of the most common drugs against different types of cancer (haematological, thyroid, breast, ovarian, lung and liver cancer)¹⁹⁻²³. Since DOX is known for certain drug resistance and side effects²⁴⁻²⁷, an efficient and sensitive detection of the amount of DOX in various types of biological samples, potentially at the point-of-care, has significant value. Recently, DOX has been loaded on graphene oxide and other nanocomposites²⁸⁻³². Regular Raman microscopy, as well as surface enhanced Raman spectroscopy (SERS) were used to detect DOX in various cell lines and real samples³³⁻³⁸. Here, optical signaling of the presence of DOX (deposited from solution) is demonstrated via three independent channels: (1) graphene enhanced Raman spectra (GERS) of DOX, (2) Raman shift of monolayer graphene (MLG) and (3) photoluminescence (PL) shift of single layer MoS₂ (Fig.1).

Currently, two major approaches are implemented in biosensor technology: label-free and label-based sensing. While the latter shows high selectivity limited only by our ability to find a high-optical-contrast receptor with best binding to known analyte, the former is much more versatile, especially in terms of sensing a wide range of analytes, enabling agnostic biosensing, and being capable to detect yet unknown biothreats for which the receptors have not been developed. Though very promising, label-free biosensors require additional calibration due to lower specificity. To solve the problem sensing multiplexing, combined with machine learning, has been applied³⁹⁻⁴¹.

In order to achieve multiplexed detection, arrays of different sensors could be integrated in one device⁴². To avoid unnecessary complexity of integration, multimodal sensing materials and heterostructures are developed⁴³⁻⁴⁶. Here we demonstrate multiplexed detection of doxorubicin by vertical heterostructure of monolayer graphene/transition metal dichalcogenide (TMDC) by measuring response of 2D materials in 3 optical channels: MoS₂ photoluminescence, graphene Raman shift and graphene enhanced Raman scattering of molecular fingerprint modes of the molecule itself.

TABLE II. Measured GERS enhancement factors for major fingerprint Raman lines of DOX

Raman line position, cm^{-1}	1236	1244	1260	1268	1326	1434	1613
GERS enhancement factor	6.4	7.0	23.3	23.3	1.8	2.9	2.1

II. RESULTS AND DISCUSSION

Label-free detection of Doxorubicin

Molybdenum disulfide, a typical TMDC 2D material, is known to show strong PL signal⁴⁷ which can be modulated by adsorption of molecular species⁴⁸⁻⁵⁴. Fig.1(c) shows a profound change in PL spectrum of MoS₂ photoluminescence (PL) after incubation to 172 nM solution of DOX for 15 minutes (the large area integrated PL is presented here; to not be confused with local micro-PL discussed below). In order to understand physical mechanisms resulting in the DOX recognition, the PL band is fitted with individual excitation lines: as shown in the inset of Fig.1(d), the MoS₂ optical transitions include typical B- and A-exciton subbands, trion (X⁻) and, often, additional localized modes. Here the shift in mode peak position ($\Delta\omega$), peak intensity (ΔP) and width ($\Delta\gamma$) are indicative for analyte absorption, resulted in subsequent charge transfer/doping and strain imposed in the 2D material. These shifts are specific for an analyte: panel (d) and data in Table I provide the values for DOX analyte. While upper B-exciton is barely influenced by the drug molecules (a small intensity difference is detected, see red arrow in panel (d)), both A-exciton and trion are red-shifted, have lower intensity and larger peak width, that all together lead to the spectral differences in panel (c). The ability to detect DOX at a low (sub-nM) concentration (and differentiate it from other components of a complex solution) would depend on amount of signal over the noise for the biosensor. Importantly, the variation of the signal in the pristine biosensing material adds to the total uncertainty and reduces the device performance as we discuss below.

Agnostic detection of a chemical or biotreat requires multiplexing the receptor signal with additional channels, as there is no calibrated negative control for unknown analyte. In order to differentiate the signal from DOX against any other molecule potentially causing PL modulation, we measure the characteristic fingerprint Raman spectrum of DOX. Fig.1(b) shows the Raman spectrum of DOX/DMSO solution (cyan curve). However, DOX Raman lines (highlighted by red arrows) are mixed, superimposed and even obscured with DMSO (background) response (cyan arrows). Furthermore, the line intensity of analyte would be comparable to background even at a relatively high DOX

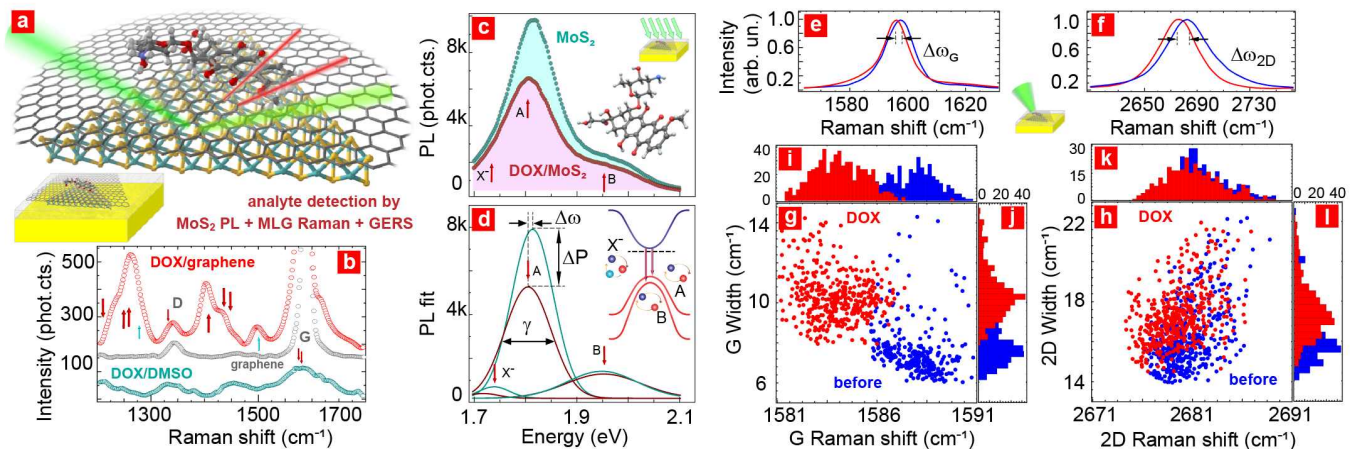


FIG. 1. Multiplexed detection of doxorubicin drug. (a) Schematics of multimode detection by the combination of MoS₂ photoluminescence, DOX GERS, and Raman shift of monolayer graphene. (b) GERS signal of DOX/MLG (red), vs. reference Raman spectra of DOX/DMSO solution (cyan) and MLG (gray); red (cyan) arrows mark DOX (DMSO) lines. (c) Modulation of MoS₂ PL spectrum: with DOX (red) and w/o DOX (cyan); inset shows DOX molecular structure. (d) Fitting of measured PL spectra from (c): A/B-exciton and trion (X⁻) lines are shown; modulation of peak position ($\Delta\omega$) and intensity (ΔP) are indicated using A-exciton fit; inset shows the schematics of optical subbands of MoS₂. (e-f) Typical Raman spectra of MLG: with DOX (red) and before incubation (blue); G- and 2D-line intensities were normalized to unity. (g-h) Correlation plots and (i-l) partial distribution functions for peak position and width for G- and 2D-lines, measured locally, at diffraction limited spots across the sample; same color code as in (e-f); clear line red-shift and broadening are detected with DOX.

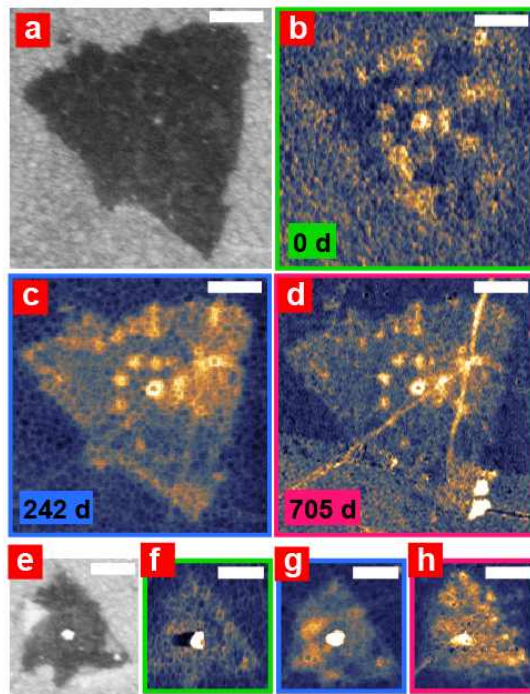


FIG. 2. Stability test of MoS₂/graphene vertical heterostructure. SEM (a,e) and sSNOM (b-d,f-h) images of two MoS₂ islands, randomly selected, coated with monolayer graphene. The island (a) shows nearly zero degradation after 242 days in ambient – from (b) to (c), neither after 705 days – from (b) to (d); the island (e) was selected near a tear in MLG and shows (g) partial oxidation near the central micro-crystallite of molybdenum after 242 days, followed by (h) almost complete oxidation of MoS₂ surface after 705 days. All scale bars are 1 μm .

concentration. On contrary, when deposited on graphene surface, most of DOX lines become clearly visible, due to a significant GERS enhancement of the Raman signal of DOX (compare red and cyan curves). Table II summarizes the amount of signal enhancement for particular lines. In our sample with only two substances, the intensity of fingerprint lines of DOX already allows to confirm the analyte structure and determine the presence of analyte (which cannot be found from a PL data channel alone). While in general, for an agnostic biosensor, the whole Raman spectrum should be analyzed by machine learning correlation analysis of the data. Here, GERS, the second data channel, complements the PL detection which can provide information of the concentration of the drug (while the intensity of the GERS signal depends on enhancement factors and cannot be used to measure the amount of analyte).

As Fig.1(b) shows, several DOX lines are superimposed with the Raman spectrum of graphene (gray curve corresponds to MLG reference), specifically with D- and G-lines near 1350 and 1600 cm^{-1} . While obscuring some of the DOX modes, Raman spectra of graphene should be analyzed separately, yielding yet another channel, to be multiplexed with the PL and GERS data. Fig.1(e-f) shows pronounced red-shift and the width increase for two major lines of graphene, G- and 2D-band, upon interaction with the DOX analyte (red). Panels (g-l) show detailed statistical information on modulation of both line position and width for both modes; in contrast with previous optical data, each data point in this figure corresponds to a small local region on the sample, less than 0.1 μm^2 , diffraction limited. Clearly, the data points aggregate in two separate clusters, though, point-to-point variability due to non-uniformity of the signal is non-negligible for 2D-mode (compare $\Delta\gamma/\Delta\omega$ correlation plot in panel (h) and partial distribution functions in panels (k-l)). Statistical distribution of the data from (g-l) contains important information about the material/sample, which will be elaborated in detail next.

Stability of 2D van der Waals heterostructure materials

Electron microscopy of MoS₂/graphene vertical heterostructure, fabricated as described in Methods, reveals structural non-uniformities. A few typical images of several randomly selected single layer MoS₂ islands, coated with MLG, are shown in Fig.2(a,e) and Fig.3(e). White nanocrystallites, likely made of insulating molybdenum oxide, charged under e-beam, are seen either in the center of the island (metal nucleation site) or at the edge (metal precipitation site); in some cases those grow to microcrystals of Mo₂O₃ (see Fig.2(e)) of characteristic triangular (or rectangular,

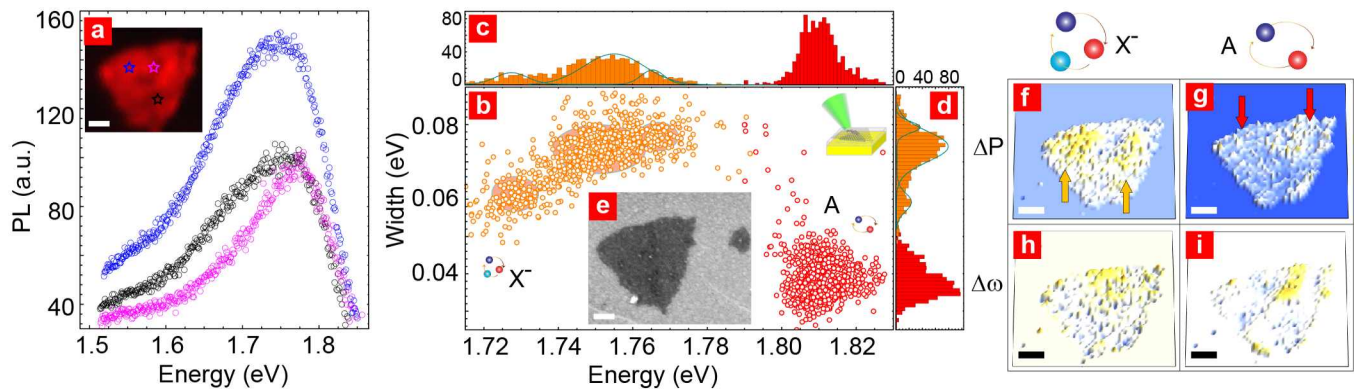


FIG. 3. Local PL characterization of MLG/MoS₂ heterostructure. (a) Single-point PL spectra of the MoS₂ island in (e). (inset) Total PL intensity map; stars show locations for the point spectra of the same color in main panel. (b) Correlation plots and (c-d) partial distribution functions for peak position and width for A-exciton (red) and trion (orange) lines, measured locally; several clusters are visible in trion data, highlighted by ovals in correlation plot and Gaussian envelope curves in distributions. (f-i) Confocal maps of MoS₂ PL: (top row) fitted intensity and (bottom row) peak position for (left) trion and (right) A-exciton; arrows show regions of higher PL intensity for trion (lower for A-exciton). All scale bars are 1 μm .

not shown here) shape and size up to 1/2 micrometer. Graphene seems to be conformal to the substrate, making short wrinkles between nanoscale posts (10-20 nm tall).

While the surface of MoS₂ islands appears mostly uniform in scanning electron microscopy (SEM) image, optical properties of 2DM demonstrate substantial variation in agreement with Raman and PL statistics from Fig.1 and Fig.3. The variability of PL in pristine material could produce uncertainty in detection of the analyte. In order to find the origin for such a variation, scattering scanning near-field optical microscopy (sSNOM) has been applied. Careful alignment of large area scans of the same heterostructure allows us to correlate different characterization channels (including SEM, scanning probe imaging, as well as PL and Raman microscopy, having a lower resolution though). In Fig.2(b-d) the sSNOM image (2nd harmonic optical amplitude, see Methods for details) reveals variation of surface impedance of MLG/MoS₂ heterostructure at the sub-micrometer scale, not captured by SEM (or AFM). We argue that a series of bright regions (on the darker background of MoS₂) correspond to the local defects of the TMDC material. Indeed, we regularly observe such a contrast at the edge of the island which is known to be prone to partial oxidation. Similar regions in the bulk of the island should correspond to concentrated sulfur vacancies, reactive to oxygen, and formation of oxy-sulfate regions, often appearing as nanoscale posts that ruckle graphene around (a near-field phase image in Fig.5(h) has the best contrast which allows to resolve nano-posts). The series of maps in Fig.2(b-d) and (f-h) show evolution of such regions protected (or non-protected) by graphene coating: the larger island (a), covered with intact MLG, preserves the same number of partially oxidized regions after nearly 2 years in ambient, except for a small oxide crystal grown in the bottom right corner, where a trench in graphene (dark line) opens an access to the air. On contrary, the small island (e) has the MLG coating cracked; as a result, the surface is slowly oxidized over the course of retention period, almost entirely on the map in panel (h). sSNOM mapping also shows that the large graphene wrinkles (bright diagonal lines in panel (d)) do not lead to alteration of optical properties. On the opposite, the oxy-sulfate regions will be shown to generate non-uniform doping of the MoS₂ and (graphene), leading to the PL variability over the sample.

Local fluctuations of PL in the pristine material were analyzed in another island of the same 2DM vertical heterostructure mapped by SEM in Fig.3(e) and in Fig.4(b) and Fig.5(h) by sSNOM. Several features are clearly resolved: graphene ruptures (not reaching the island), an oxide crystallite at the edge of the island, a few oxy-sulfate nano-posts and graphene wrinkles around the posts, and several regions of darker SEM contrast (likely, more conductive than bare MLG), potentially indicating doping/Fermi level variation. Confocal PL image of the same area is presented in Fig.3(a), inset. The large non-uniformity of PL intensity is followed by substantial variability of PL line shape (cf. the curves in main panel taken at three locations shown in the inset). Similar to the large area PL data in Fig.1(c), the main variability of micro-PL results from the A and X⁻ states, to be analyzed separately. Panel (b) presents the correlation plot for fitted PL peak position and width for A-exciton (red) and trion (orange) states by the local optical probe on the surface of MLG/MoS₂ heterostructure shown in Fig.3(e). MicroPL reveals large non-uniformity in optical signal. Trion partial distribution functions for both $\Delta\gamma$ and $\Delta\omega$ show 3 major clusters (highlighted by ovals in panel (b) and green curves in (c-d)), that correspond to the regions of heterostructure where materials properties are locally modulated.

Maps in panels (f-i) show actual distribution of the peak position, $\Delta\omega$, and peak intensity, ΔP , with diffraction

limited resolution. Importantly, the intensity maps show the anti-correlation for PL strength of A-exciton and trion (as indicated by red and orange arrows): the trion PL is the highest where the A-exciton PL is depressed, compare locations for trion-dominated (blue/black) and exciton-dominated (purple) PL curves in panel (a). Such a correlation may result from non-uniform doping of the MoS₂ island. Indeed, in a highly-doped area the neutral excitons are bound to free charges and, thus, converted into trions⁴⁸.

Multidimensional characterization of heterostructure materials

Although useful to shed the light on the PL variability, the confocal PL characterization neither has enough spatial resolution nor enables assessing the MoS₂ doping level to uncover the mechanisms of non-uniform optical signaling. Instead, we developed a multidimensional imaging combining sSNOM and Kelvin probe force microscopy (KPFM) to be correlated with PL (and Raman) microscopy. In Fig.4(a-b) two maps of the same island – using KPFM (work function) channel and sSNOM (optical surface impedance) channel – show identical contrast, further detailed in panel (c) where the cross section profiles allow to quantify the variation of the Fermi level of graphene above the MoS₂ layer. The profile of work function is schematically shown in Fig.4(h). Charge transfer in the vertical heterojunction decreases the carrier density in both graphene and MoS₂ underneath, thus, decreasing the magnitude of graphene work function and doping level. The KPFM probe is in contact with the outermost layer of the heterostructure, graphene, thus it measures the work function of MLG. Graphene above the island appears negatively doped by MoS₂. The MLG Fermi level, taken with respect to graphene Dirac point, is negative, corresponding to p-doping. Statistical distribution of the Fermi level values of graphene on/off the island is shown in panel (f) by red/green histogram. Knowing E_F in bare graphene and in the vertical heterostructure allows us to calculate the MoS₂ doping level, Fig.4(d). Using median values for E_F , it can be estimated to lie in the range $1 - 25 \times 10^{12} \text{ cm}^{-2}$, which is further corroborated by independent Raman data below.

Comparison of KPFM and sSNOM profiles in Fig.4(c), as well as the distribution functions in Fig.4(f-e), allows to calibrate the near-field signal in terms of the Fermi level of the heterostructure. Then, one could interpolate the charge transfer/doping data to the nanometer features, only resolved by sSNOM (such as wrinkles, oxy-sulfate regions, etc.), and thus, determine the origin for PL non-uniformity.

Enhanced resolution of sSNOM allows us to determine 5 sources of non-uniform doping in the vertical van der Waals heterostructures as shown schematically in Fig.4(h). (i) The primary doping is defined by conditions of the MoS₂ synthesis: it is known that often the stoichiometry of TMDC is slightly off the equilibrium values. Deficiency in sulfur leads to creation of surface vacancies, typically resulting in n-doping⁵⁵. (ii) Filling of the S-vacancy with oxygen or CH-group yields weaker n- or p-doping^{48,56}, which was shown to be localized near the defect site⁵⁷. (iii) In Mo-abundant synthesis, small micro-crystallites of metal molybdenum form, later oxidized to MoO_x, or forming MoO_xS_y domains. (iv) In the heterostructure, work function and/or Fermi level difference between the layers results in charge transfer between the layers. Typically p-doped MLG would become an acceptor for electrons transferred from n-doped MoS₂. Finally, (v) the Si/SiO₂ substrate supports the heterostructure, which is known to have a high density of traps at the interface. Such traps, if charged, produce a substantial field and shift of the Fermi level in all 2DM layers above it, generating a random Coulomb potential for charge carriers both in MoS₂ and graphene.

Additional evidence for the existence of defects/vacancies in TMDC lattice is provided by high-angle annular dark-field (HAADF) Scanning Transmission Electron Microscopy (STEM) imaging. Fig.5(e) shows atomic resolution map of a typical MoS₂ island. The boundary between dark area and the lower contrast area likely reflects the grain boundary which separates regions of different lattice orientation. Such a twin boundary produces strain and may result in localization of electronic states. Furthermore, several (3-fold) individual defects are seen in the STEM image (approximately half a dozen per 200 nm² which corresponds to ca. $3 \times 10^{12} \text{ cm}^{-2}$).

Multiple sources of optical non-uniformity, stemming from the variation of the doping level, have been further studied with micro-Raman imaging: typical Raman spectra of MLG/MoS₂ heterostructure are shown in Fig.5(a,c). Panel (a) presents A- and E¹-modes of MoS₂ layer, A-intensity map is shown in inset (b). Mode frequencies, fitted as in (a), allow to determine the strain and doping⁵⁸ of the island underneath the graphene, see Methods, generating the maps presented in panels (f,g). Consistent with the KPFM data, Fig.4(a), MoS₂ doping is lower along the vertical axis of the island, thus, both the amount of charge transfer and graphene E_F should be lower. Charge doping and strain in graphene have been calculated using a similar procedure^{59,60}. Upper/lower curves in panel (c) correspond to MLG Raman lines off/on TMDC, where the location of the island is clearly seen, *e.g.*, in the map of 2D-amplitude (d). Fig.5(i,j) show graphene doping and isotropic/hydrostatic strain. Furthermore, the splitting of the G- and 2D-doublet modes (see the fitted curves in panel (c)) yields⁶¹ the shear (non-isotropic) component of the strain, panel (k).

High-resolution map reveals that the hole carrier density in graphene increases next to the location of a large MoO_x crystallite, which should indicate additional chemical doping. Besides doping, all nanoscale features of heterostructure morphology make contributions to the uniform and non-uniform components of graphene strain, thus making Raman

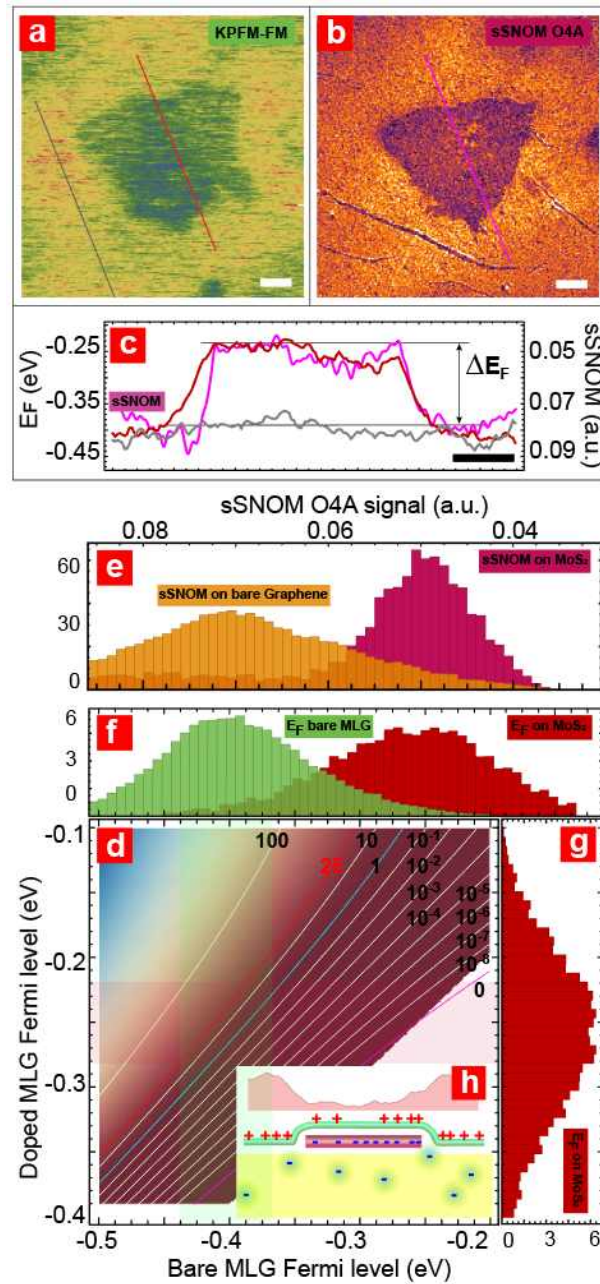


FIG. 4. Correlation of MLG work function data with sSNOM optical surface impedance. Aligned maps for (a) KPFM and (b) sSNOM (4th harmonic) amplitude. (c) Cross section profiles across the MoS₂ area (KPFM, red and sSNOM, pink) vs. MLG reference (KPFM, gray), taken along the lines of the same color in (a-b). (d) Calculated electron density in MoS₂ heterostructure, log-scale, vs. Fermi levels in bare/doped graphene off/on the island. (f-g) Partial distribution functions for measured E_F in bare graphene (off island, green) and graphene doped by the MoS₂ (on island, red) from KPFM map in (a). (e) Partial distribution functions for sSNOM signal from (b) to calibrate near-field signal by E_F . Note common abscissa axis for panels (d,f), not (e). Inset (h) shows schematics of charge transfer in the vertical heterojunction on SiO₂ substrate with negative charge traps. Pink curve outlines the variation of MLG work function. All scale bars are 1 μm .

line width larger than the natural width⁵⁹, due to the statistical broadening.

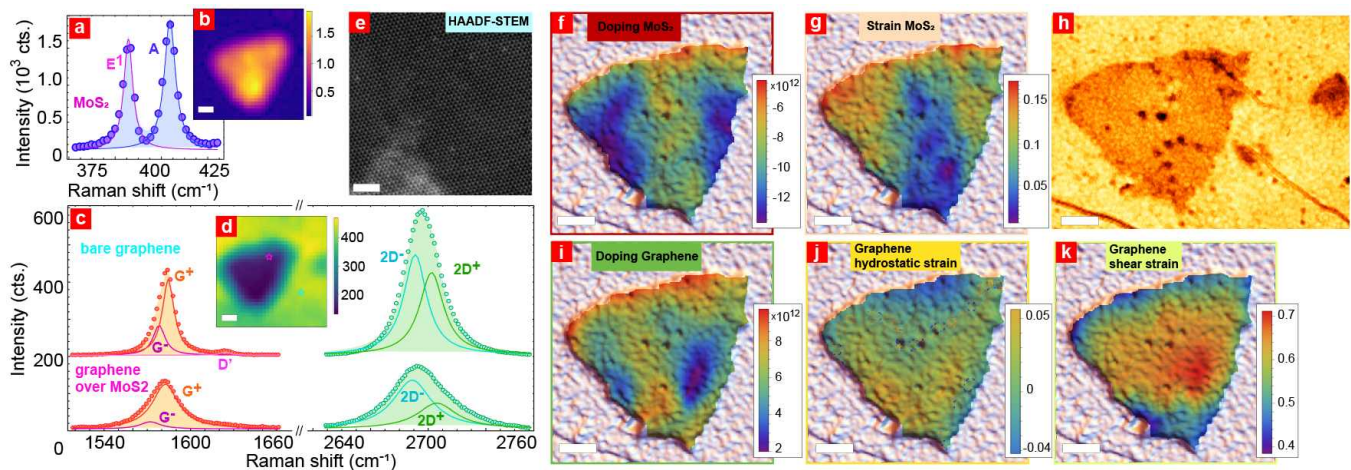


FIG. 5. Raman mapping of doping and strain non-uniformity in the heterostructure. (a) Typical MoS₂ Raman spectrum, fitted with E¹ and A-lines. (b) A-line intensity map. (c) Typical Raman spectra for MLG off/on MoS₂ island, fitted by G (orange), D' (pink) and 2D (green) lines; splitting of G- and 2D-lines is shown in the fit. (d) Raman map of 2D-amplitude showing the island location, cf. map in (b). (e) HAADF-STEM image of MoS₂ lattice: notice grain boundaries and individual defects; scale bar is 2 nm. (f,g) Calculated doping and strain for MoS₂ layer overlaid with SEM map; (h) sSNOM phase image of the same area; (i-k) MLG doping, hydrostatic and shear strain maps. All scale bars, except in (e), are 1 μm .

A. Outline

Cumulatively, multidimensional characterization data above revealed existence of non-uniformities in 2D materials at the nanoscale and allowed to identify doping and/or strain variations as the origin of statistical distribution of the optical signals used in all three recognition channels (PL shift, Raman spectroscopy and GERS). When integrated over the device area, such a variability in local response would translate in a broadening of the biosensing spectral signal, thus, raising device-to-device variability and, ultimately, lowering the sensitivity and the limit-of-detection by increasing background and/or systematic error. While the variability of individual device response often could be addressed by careful calibration against known analytes, such a fluctuation and spread of the integrated response would affect biosensing accuracy and, certainly, reduce the ability to perform precise biosensing in the agnostic detection mode. Presented study suggests that in order to improve the performance of biosensors based on 2DM heterostructures, non-uniformity of doping and strain – two major mechanisms for optical signal variation – must be addressed. Currently, most of 2DM heterostructures are fabricated by transfer methods, that are known to produce both strain and doping^{62–64} (especially for wet transfer). New methods of strain-free and doping-free transfer need to be developed^{62,65}. Alternatively, such heterostructure materials should be fabricated in-situ, in synthetic facility, to preserve the layer epitaxy and exclude contamination between the layers.

METHODS

B. Sample fabrication

The monolayer MoS₂ was grown on a Si substrate with 300 nm thick SiO₂ by Chemical Vapor Deposition (CVD) method as described in⁵⁰. Optimization of synthesis parameters and stoichiometric ratio of molybdenum to sulfur resulted in producing triangular MoS₂ islands with low defect density (cf. STEM image in Fig.5(e)), predominantly single layers, with low surface coverage. Monolayer graphene was grown by CVD on Cu foil. MLG was transferred onto MoS₂ using the conventional PMMA assisted transfer technique⁶⁶. The SEM image of resulted heterostructure is shown on Fig.3(e).

C. Sample Characterization.

SEM sample imaging was performed in a field emission scanning electron microscope Zeiss Auriga FIB/FESEM. Atomic resolution images of monolayer MoS₂ samples transferred onto Quantaifoil TEM grids were recorded using

Nion Ultra HAADF-STEM operating at 60 kV with 3rd-generation C3/C5 aberration corrector and 0.5 nA current in atomic-size probe $\sim 1.0 - 1.1\text{\AA}$ (NCATSU). Confocal PL and Raman characterization were performed using a Horiba Jobin Yvon LabRAM HR-Evolution Raman system, 488 nm (for Raman) and 532 nm (for PL) laser excitation wavelengths were used; Horiba XploRA Raman system was used for taking Raman spectra at 532 nm of excitation. Analysis of PL and Raman characterization was performed using home-written codes.

sSNOM maps were collected using scattering type scanning near-field optical microscope (custom-built Neaspec system) in pseudo-heterodyne mode (tapping amplitude ~ 70 nm, ARROW-NCPT probes by Nanoworld < 25 nm radius), excitation by CW Quantum Cascade Laser (MIRCat by Daylight) at power < 2 mW in focal aperture at $1577\text{-}1579\text{ cm}^{-1}$ ($6.333\text{-}6.341\text{ }\mu\text{m}$). Amplitude and phase of high order harmonics (≥ 2) are proportional to the local impedance of the sample under the tip.

The AFM/KPFM was performed using Dimension Icon AFM in PeakForce Kelvin Probe Force Microscopy in frequency modulated mode (PFKPFM-FM, Bruker Nano Inc., Santa Barbara, CA) utilizing a PFQNE-AL probe (Bruker SPM Probes, Camarillo, CA). Prior to measuring the samples, the KPFM response of the probe was checked against an Au-Si-Al standard and the work function of the Al reference metal layer was calibrated against a freshly cleaved highly oriented pyrolytic graphite (HOPG) reference sample (PFKPFM-SMPL, HOPG-12M, Bruker SPM Probes, Camarillo, CA); 4.6 eV was used for the work function reference value for HOPG.

D. Supporting Information

Supporting Information is available from the Wiley Online Library or from the author.

ACKNOWLEDGMENTS:

Authors are personally thankful to Drs. T. Tighe, T. Williams and M. Wetherington (MCL, PSU). S.V.R. acknowledges NSF support (CHE-2032582). T.I. and K.S. acknowledges NSF support (CHE-2032601). T.I. acknowledges Sample Grant from The Pennsylvania State University 2DCC-MIP, which is supported by NSF cooperative agreement (DMR-1539916). Work at PSU sSNOM facility has been partially supported by NSF MRSEC (DMR-2011839). Part of this work was performed at the Joint School of Nanoscience and Nanoengineering (JSNN), a member of the Southeastern Nanotechnology Infrastructure Corridor (SENIC) and National Nanotechnology Coordinated Infrastructure (NNCI), which is supported by the NSF grant (ECCS-1542174). Scanning Transmission Electron Microscope imaging was conducted at the Center for Nanophase Materials Sciences at ONRL, which is a DOE Office of Science User Facility.

SUPPLEMENTARY INFORMATION

III. STRAIN AND DOPING ANALYSIS

The background signal of Raman spectra for monolayer graphene (MLG) was fit and subtracted using air PLS⁶⁷. Then peaks were fit for both MLG and TMDC spectra using the non-linear least-squares minimization and curve-fitting library (LMFIT) for python. Peaks were fit using Lorentzian line shapes around the D, G^+ , G^- , $2D^+$ and $2D^-$ peaks, as well as around nearby shoulder peaks if they were distinguishable.

The initial separation of strain and doping is accomplished by examining the central peak position of the 2D and G line fits. These Raman frequencies are sensitive to both strain and doping because of the change in lattice constants and force fields that effect the phonon frequencies. Lee et al. created a procedure for extracting the strain and doping of graphene through the statistical analysis of the changes in the Raman frequency position⁶⁸. By plotting the 2D and G peaks against each other we are able to see trends in the spectra which represent modulation either by strain or by doping, or both. Strain is seen in the MLG Raman data as a cluster in of the 2D/G correlation plot (Figure 6) with a linear slope of approximately 2.2. The linear slope for p-doped MLG is approximately 0.75 which is also seen in Figure 6. At very low values of p-doping and n-doping the dependence should be nonlinear, though, due to Fermi velocity (density of states) renormalization.

It is known that graphene on MoS_2 and SiO_2 substrate is typically p-doped. Assuming linear correlation with

Raman frequencies, we can extract the relative change in strain and doping by solving the linear equation system:

$$\begin{pmatrix} \omega_G \\ \omega_{2D} \end{pmatrix} = \begin{vmatrix} a_{G,\varepsilon} & a_{G,\rho} \\ a_{2D,\varepsilon} & a_{2D,\rho} \end{vmatrix} \begin{pmatrix} \varepsilon \\ \rho \end{pmatrix} \quad (1)$$

Where the vector (ω_G, ω_{2D}) should be calibrated against unstrained and undoped graphene reference sample.

Graphene has two different polarizations of optical modes that are degenerate at zero strain. Depending on the axial direction of (uniaxial) strain, position of one of the modes shifts with respect to the other one. This generates a Raman doublet for general strain. Knowing a particular strain configuration is only possible with Raman mapping in

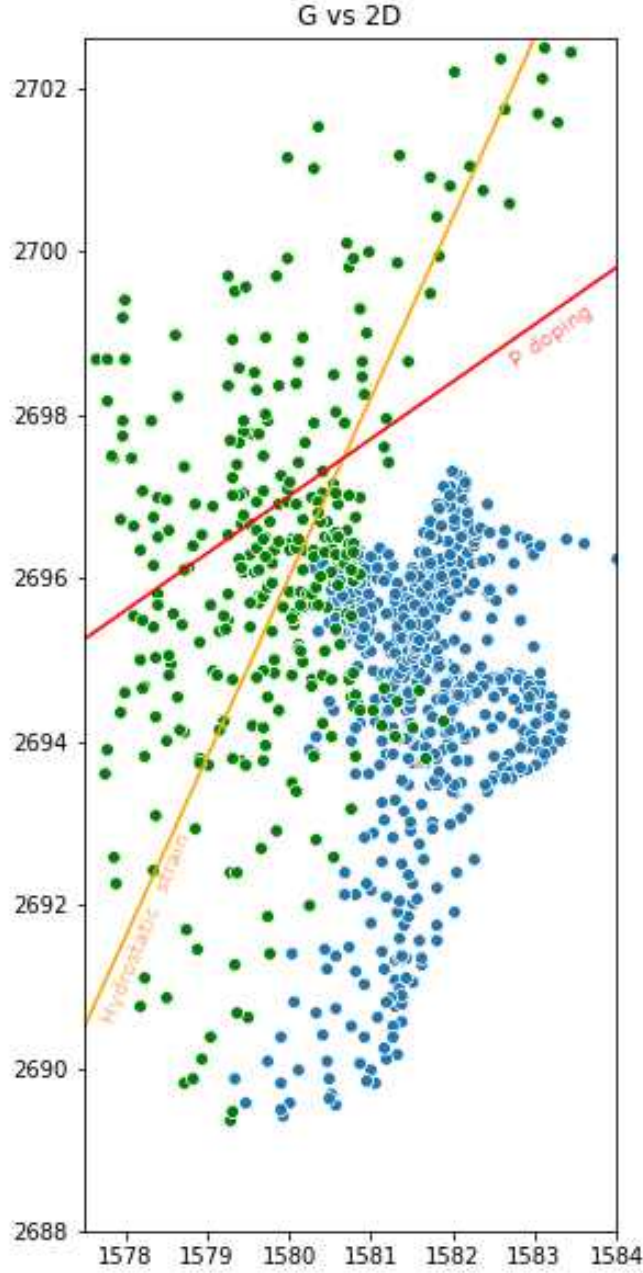


FIG. 6. G vs 2D plot showing the split of graphene on the bare SiO₂ substrate (light blue) and over MoS₂ island (green). Red/yellow line indicates a characteristic slope for G-2D data correlation caused by pure doping/strain (isotropic biaxial).

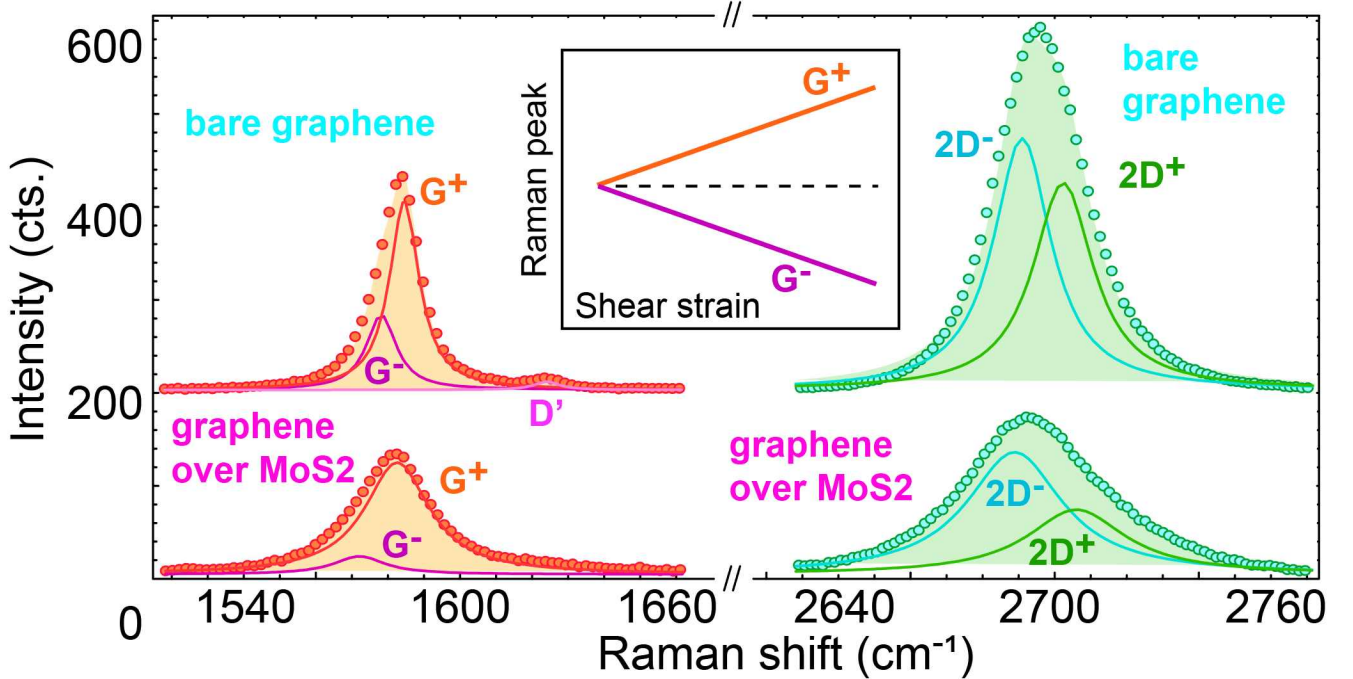


FIG. 7. Main figure reproduces the data from Fig. 5c: the dots and filled line represent the experimental data and the total fitted curve. The individual components of the doublet are shown with the thin lines. Additional D'-component is needed for fitting the spectrum in vicinity of the G-doublet for bare graphene. (inset) Schematics of G-line splitting with the shear strain. Hydrostatic strain, on contrary, shifts the whole doublet but does not influence the splitting.

polarized light, which resolved the polarization of a phonon mode. However, even in the case of non-polarized Raman data, position of individual components of the doublet allows to separate the isotropic and anisotropic components of the strain. The latter corresponds to the shear strain, although in order to determine specific shear direction, a polarized spectroscopy will be required, also on a calibration sample with know lattice orientation.

Mueller et al. developed a formalism to separate the doping and hydrostatic strain and shear strain components⁶⁰. Critically, the shear strain component does not change the strain/doping correlation, that is, the slope of the curves in Figure 6. While the hydrostatic component does not affect the splitting of the 2D or G peaks into doublet, as it shown on Figure 7. The amount of the splitting allows us to determine the magnitude of the shear strain, while the magnitude of the hydrostatic strain can be determined by examining the averaged peak position (after splitting). We can then determine the magnitude of the strain components and the doping by examining the shift of the peaks in a “zero strain” case or a “zero doping” case. Parametrization follows the paper by Das et al.: in the undoped case the 2D peak shifts at a rate of 1.04 cm^{-1} per 10^{12} cm^{-2} hole density⁶⁹. We use 2D splitting data and the Grueneisen parameter and the shear deformation potential from⁶⁰ to determine the strain components from:

$$\omega_{2D}^{\pm} = \langle \omega_{2D} \rangle (-\alpha \varepsilon_h \pm \beta \varepsilon_s) \quad (2)$$

where $\alpha = 1.8$ is the Grueneisen parameter for MLG, and $\beta = 0.99$ is the shear deformation potential.

The strain and doping of MoS₂ can also be determined from Raman correlation data (Rao et al.2019). Peaks for MoS₂ were fit in the same way as the graphene peaks (Figure 10). For the case of MoS₂ we compare E peak and A peak that are near 382 and 404 cm^{-1} respectively. The E peak position is more sensitive to strain, similar to the 2D peak of MLG, while the A peak position is more sensitive to doping, like the G peak of MLG. The slope for strain correlation is ~ 4 ; the slope for doping is ~ 0.12 . We can then use the undoped E peak position, and a Grueneisen parameter for MoS₂ of ~ 0.86 , to obtain the average strain. Then we examine the unstrained A peak position which shifts at a rate of 4 cm^{-1} per $1.8 \cdot 10^{13} \text{ cm}^{-2}$ ⁷⁰ and determine the doping. Unlike graphene, the peak splitting in MoS₂ is absent.

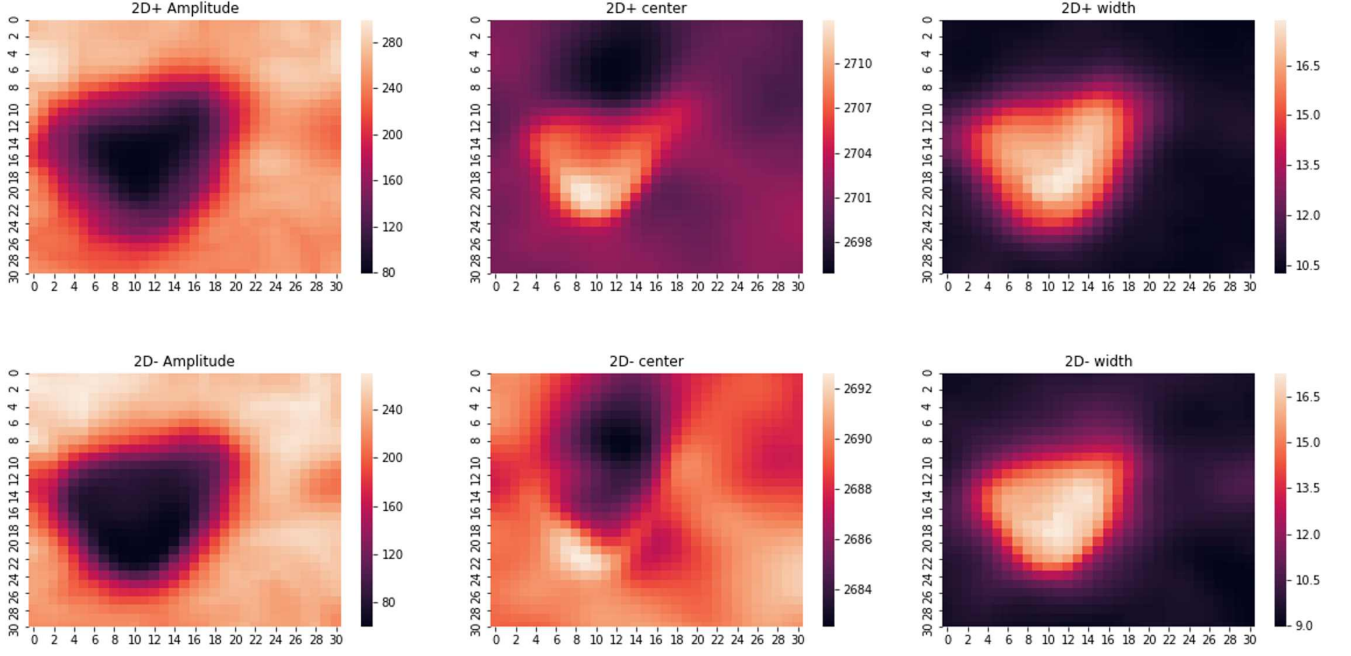


FIG. 8. The maps showing the fitted parameters for splitting of 2D peaks.

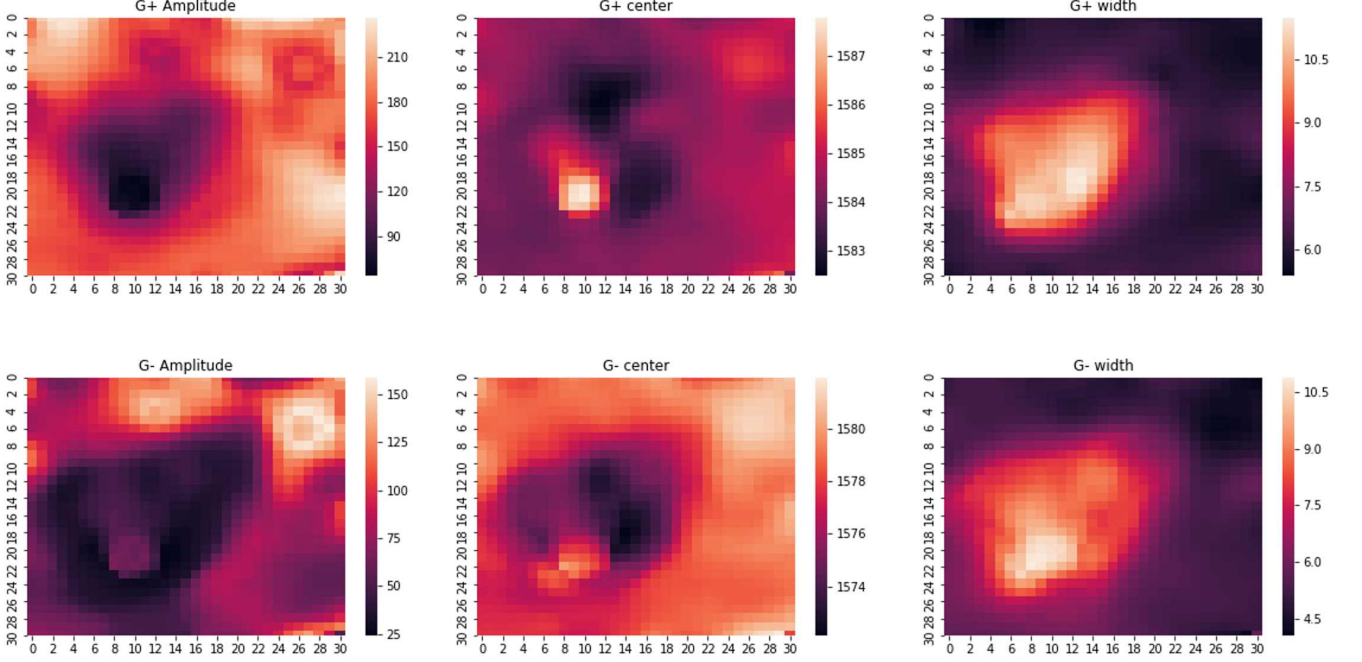


FIG. 9. The maps showing the fitted parameters for splitting of G peaks.

IV. CHARACTERIZATION BY PEAK-FORCE KEVIN PROBE FORCE MICROSCOPY (KPFM)

In general, the work function value Φ_{sample} and, consequently, Fermi level variation can be calculated from KPFM measurements using an equation:

$$\Phi_{sample} = eV_{CPD} - \Phi_{probe} \quad (3)$$

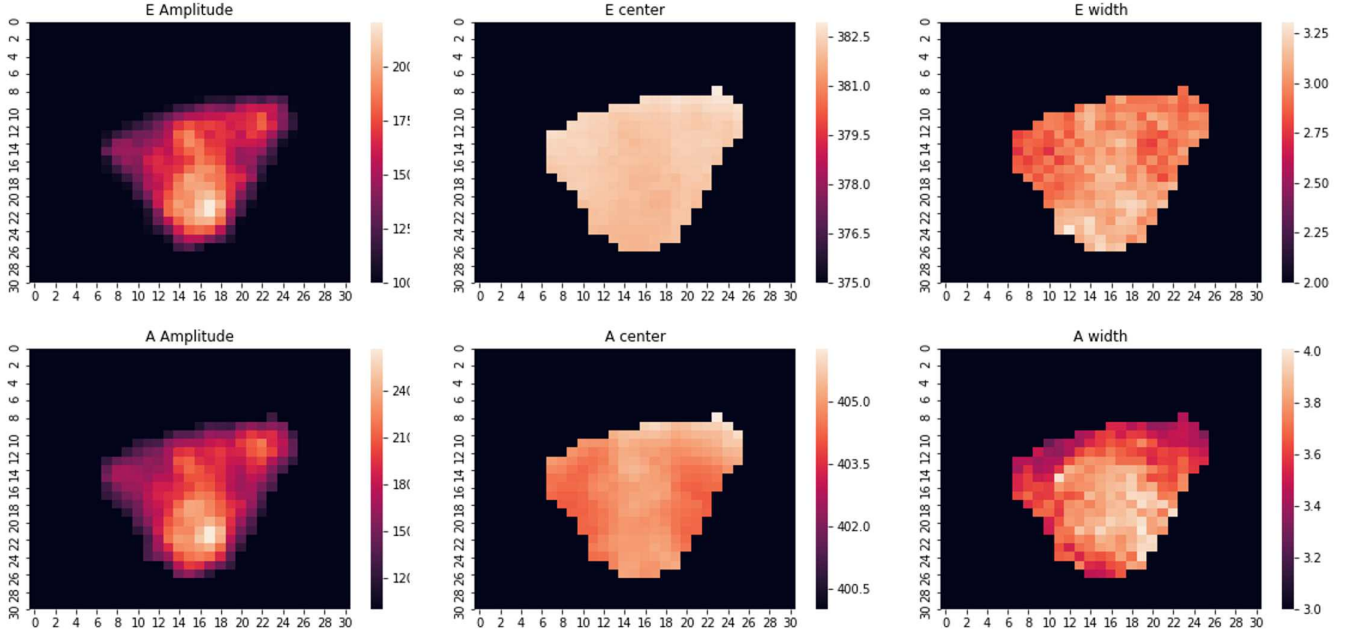


FIG. 10. The maps showing the fitted parameters for MoS₂ peaks.

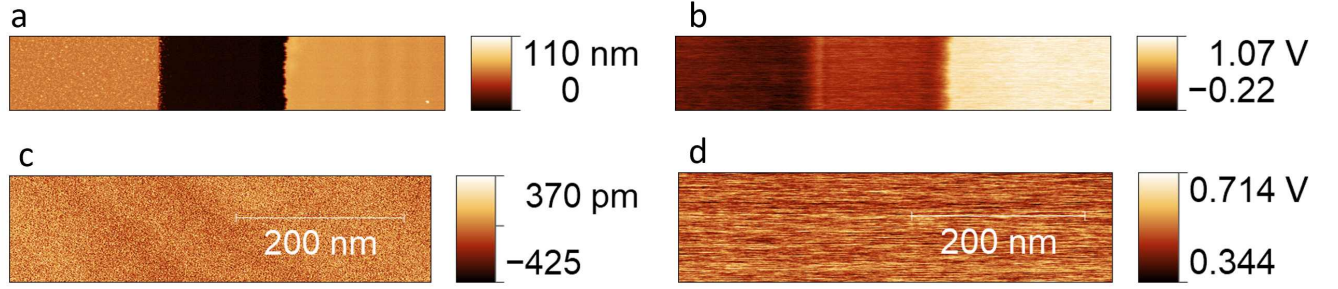


FIG. 11. (a) AFM topography and (b) KPFM signal for the Au-Si-Al standard. (c) AFM topography and (d) KPFM channel for HOPG reference sample.

where V_{CPD} is the contact potential difference between the sample and the AFM probe, e is elemental charge, and Φ_{probe} is the work function of the KPFM probe. Prior to measuring the MoS₂/graphene samples, we checked the KPFM probe response against an Au-Si-Al standard. Topography and V_{CPD} maps of standard are shown on Figure 10a,b. Next, the work function of aluminum was calibrated against a freshly cleaved highly oriented pyrolytic graphite (HOPG) reference (Figure 10c,d) using value of $\Phi_{HOPG} = 4.6\text{eV}$ (PFKPFM-SMPL, HOPG-12M, Bruker SPM Probes, Camarillo, CA). To eliminate influence of water condensation the AFM chamber was purged with nitrogen gas.

The topography of MoS₂/graphene sample (Figure 11a) is dominated by roughness of Si/SiO₂ substrate, and since the thickness of MLG and monolayer MoS₂ is below RMS, topographical details of heterostructures cannot be resolved by routine AFM imaging. The spatial distribution of V_{CPD} and calculated work function value of the same area are presented on Figure 11b,c. It must be noted that the KPFM probe is in contact with the outermost layer of the heterostructure, graphene, thus it measures the work function of MLG, Φ_{MLG} , either on or off the MoS₂ island. The work function value "off" the island reveals p-doping of graphene, likely due to transfer procedure. The Fermi level value, taken with respect to graphene Dirac point, is negative. The "on" value is shifted towards the Dirac point, showing non-uniform n-doping effect, originated from the charge transfer in the heterostructure.

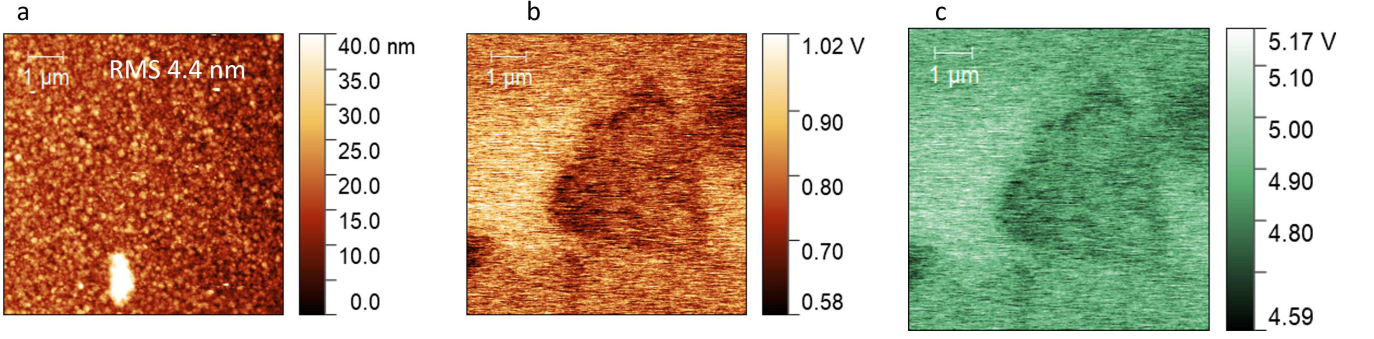


FIG. 12. The maps of a MoS₂/graphene sample: (a) AFM topography, (b) KPFM, and (c) calculated work function distribution.

V. CALCULATION OF CHARGE DENSITY IN MLG AND IN MOS₂ MONOLAYER

For 2d-materials with parabolic dispersion relation (with massive fermions), like MoS₂, the energy is given by: $E = E_c + \hbar^2 k^2 / (2m^*)$. Then, the density of states (DOS) is constant for each band: $= 2m^* / (\pi \hbar^2)$. Then, the following integral gives the carrier density dependence on the Fermi level (spin and valley degeneracy included):

$$n(F) = \frac{2m^*}{\pi \hbar^2} \int_{E_c}^{\infty} \frac{dE}{1 + \exp[\frac{E-F}{kT}]} = \frac{2m^* kT}{\pi \hbar^2} \log \left(1 + \exp \left[\frac{F - E_c}{kT} \right] \right) = N_c \log \left(1 + \exp \left[\frac{|E_c| - |F|}{kT} \right] \right) \quad (4)$$

where we assume that both Fermi level F and $E_c = -4.21$ eV⁷¹ are taken with respect to the vacuum level and, thus, are negative (this definition is consistent with the definition for Dirac point E_D , conduction band edge E_c and Fermi level F). The conduction band DOS is given by:

$$N_c = \frac{2m^* kT}{\pi \hbar^2} = \frac{2m^*}{m_o} \frac{kT}{\pi a_B^2 E_B} \simeq 7.6 \cdot 10^{12} \text{ cm}^{-2} \quad (5)$$

with m_o being the free electron mass, $a_B = 0.53$ Å, $E_B = 27$ eV, and effective mass in MoS₂ is taken to be $0.35m_o$ ⁷².

There are two limits to be noted: for non-degenerate doping ($|F| > |E_c|$, Fermi level lies below the bottom of CB), one can use $\log(1+x) \sim x$ and write:

$$n \simeq N_c \exp \left[-\frac{|F| - |E_c|}{kT} \right] \quad (6)$$

while in the degenerate doping limit ($|E_c| - |F| \gg kT > 0$, Fermi level is within the CB), unity is neglected compared to the large exponential, and we derive linear dependence of the charge density on the Fermi level:

$$n \simeq N_c \frac{|E_c| - |F|}{kT} \quad (7)$$

Correspondingly for the monolayer graphene, which is gapless with a linear dispersion relation $E = \hbar v_F k$, we derive:

$$n_g(F) = \frac{(E_D - F)^2}{\pi \hbar^2 v_F^2} = N_g (E_D - F)^2 \quad (8)$$

where the Dirac point $E_D = \chi_{MLG} \simeq -4.57$ eV⁷³, and Fermi velocity $v_F \simeq 1.16 \times 10^6$ m/s⁷⁴. We emphasize that N_g is not a density of carriers, neither it is a 2d-DOS in a classical sense: $N_g \simeq 5.46 \cdot 10^{13} \text{ cm}^{-2} \text{ eV}^{-2}$.

Since the 2d materials are electrically isolated from the Si substrate by the oxide layer, they are at floated potential and the charge transfer produces 2D charge densities $\pm en_1$, equal (by magnitude and opposite by sign) in both layers, and generates $2\delta V$, a potential difference between TMDC and MLG ($\phi(z \pm d/2) = \pm \delta V$). This potential difference is linearly proportional to the surface charge formed at each of the materials, as the result of charge transfer.

Then, the positions of the Fermi levels, both defined with respect to the higher vacuum level in MLG, are:

$$|F_g| = |F_g^{(o)}| - \Delta_F \quad |F_{MoS_2}| = |F_{MoS_2}^{(o)}| + 2\delta V + \Delta_{FMoS_2} \quad (9)$$

where the differences: $\Delta_F = F_g^{(o)} - F > 0$ is the Fermi level (up)shift in graphene, which can be measured as work function difference taken on and off the TMDC island, and Δ_{FMoS_2} , the Fermi level (down)shift in MoS₂.

Knowing the expression for TMDC and MLG DOS, one can easily calculate the charge transfer and, then, the potential difference between the layers in the vertical heterostructure. Thus, the relation between the measured MLG work function and the doping level of TMDC can be established, as shown in the Fig. 4d of main text.

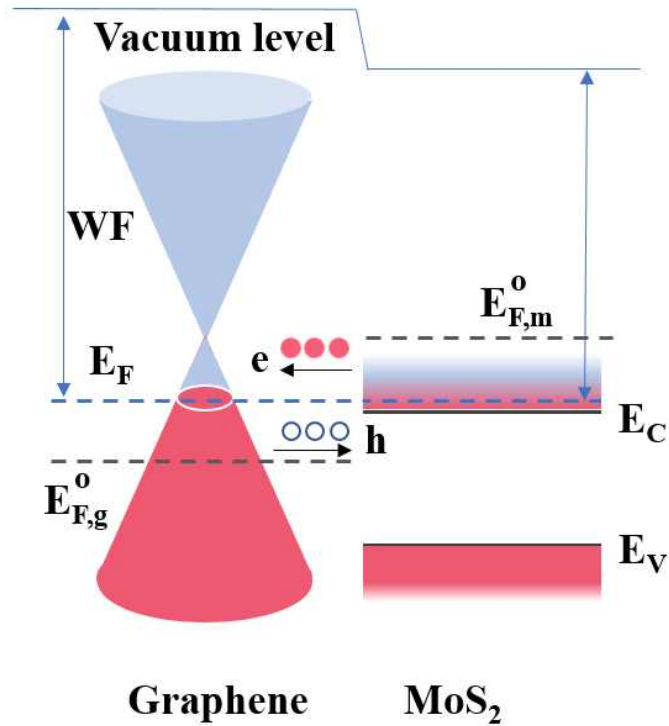


FIG. 13. Matching band structure offsets in MoS₂/graphene van der Waals heterojunction: in order to align the Fermi level, the charge transfer between the 2D-materials must happen, resulted in a drop of vacuum level between the layers.

VI. ANIMATION FILE

SI includes an animation file representing some of the channels of multidimensional characterization of a particular van der Waals vertical heterostructure (single layer MoS₂ packaged by graphene monolayer). The same area of the sample has been imaged using different instrumentation. Theoretical results on the charge transfer (doping) and various components of strain are also shown.

REFERENCES

- ¹ Kostarelos, K.; Novoselov, K. S. Graphene devices for life. *Nature Nanotechnology* **2014**, *9*, 744–745.
- ² Bolotsky, A.; Butler, D.; Dong, C.; Gerace, K.; Glavin, N. R.; Muratore, C.; Robinson, J. A.; Ebrahimi, A. Two-Dimensional Materials in Biosensing and Healthcare: From In Vitro Diagnostics to Optogenetics and Beyond. *ACS Nano* **2019**, *13*, 9781–9810.
- ³ Zhu, X.; Ding, R.; Wang, Z.; Wang, Y.; Guo, X.; Song, Z.; Wang, Z.; Dong, M. Recent advances in synthesis and biosensors of two-dimensional MoS₂. *Nanotechnology* **2019**, *30*, 502004.
- ⁴ Daus, A.; Vaziri, S.; Chen, V.; Koroglu, C.; Grady, R. W.; Bailey, C. S.; Lee, H. R.; Schauble, K.; Brenner, K.; Pop, E. High-performance flexible nanoscale transistors based on transition metal dichalcogenides. *Nature Electronics* **2021**, *4*, 495–501.
- ⁵ Lee, J.; Dak, P.; Lee, Y.; Park, H.; Choi, W.; Alam, M. A.; Kim, S. Two-dimensional Layered MoS₂ Biosensors Enable Highly Sensitive Detection of Biomolecules. *Scientific Reports* **2014**, *4*, 7352.
- ⁶ Campuzano, S.; Pedrero, M.; Nikoleli, G.-P.; Pingarron, J. M.; Nikolelis, D. P. Hybrid 2D-nanomaterials-based electrochemical immunosensing strategies for clinical biomarkers determination. *Biosensors and Bioelectronics* **2017**, *89*, 269–279.
- ⁷ Oh, S.-H.; Altug, H.; Jin, X.; Low, T.; Koester, S. J.; Ivanov, A. P.; Edell, J. B.; Avouris, P.; Strano, M. S. Nanophotonic biosensors harnessing van der Waals materials. *Nature Communications* **2021**, *12*, 3824.
- ⁸ Pang, Y.; Yang, Z.; Yang, Y.; Ren, T.-L. Wearable Electronics Based on 2D Materials for Human Physiological Information Detection. *Small* **2020**, *16*, 1901124.
- ⁹ Yen, C.-W.; de Puig, H.; Tam, J. O.; Gomez-Marquez, J.; Bosch, I.; Hamad-Schifferli, K.; Gehrke, L. Multicolored silver nanoparticles for multiplexed disease diagnostics: distinguishing dengue, yellow fever, and Ebola viruses. *Lab Chip* **2015**, *15*, 1638–1641.
- ¹⁰ Wang, S.; Li, X.; Chen, Y.; Cai, X.; Yao, H.; Gao, W.; Zheng, Y.; An, X.; Shi, J.; Chen, H. A Facile One-Pot Synthesis of a Two-Dimensional MoS₂/Bi₂S₃ Composite Theranostic Nanosystem for Multi-Modality Tumor Imaging and Therapy. *Advanced Materials* **2015**, *27*, 2775–2782.
- ¹¹ Lee, H.; Choi, T. K.; Lee, Y. B.; Cho, H. R.; Ghaffari, R.; Wang, L.; Choi, H. J.; Chung, T. D.; Lu, N.; Hyeon, T.; Choi, S. H.; Kim, D.-H. A graphene-based electrochemical device with thermoresponsive microneedles for diabetes monitoring and therapy. *Nature Nanotechnology* **2016**, *11*, 566–572.
- ¹² Lei, Y.; Zhao, W.; Zhang, Y.; Jiang, Q.; He, J.-H.; Baumner, A. J.; Wolfbeis, O. S.; Wang, Z. L.; Salama, K. N.; Alshareef, H. N. A MXene-Based Wearable Biosensor System for High-Performance In Vitro Perspiration Analysis. *Small* **2019**, *15*, 1901190.
- ¹³ Zhang, B.; Pinsky, B. A.; Ananta, J. S.; Zhao, S.; Arulkumar, S.; Wan, H.; Sahoo, M. K.; Abeynayake, J.; Waggoner, J. J.; Hopes, C.; Tang, M.; Dai, H. Diagnosis of Zika virus infection on a nanotechnology platform. *Nature Medicine* **2017**, *23*, 548–550.
- ¹⁴ Zhang, Y.; Zheng, B.; Zhu, C.; Zhang, X.; Tan, C.; Li, H.; Chen, B.; Yang, J.; Chen, J.; Huang, Y.; Wang, L.; Zhang, H. Single-Layer Transition Metal Dichalcogenide Nanosheet-Based Nanosensors for Rapid, Sensitive, and Multiplexed Detection of DNA. *Adv. Mater.* **2015**, *27*, 935–939.
- ¹⁵ Wang, Y.; Tang, L.; Li, Z.; Lin, Y.; Li, J. In situ simultaneous monitoring of ATP and GTP using a graphene oxide nanosheet-based sensing platform in living cells. *Nature Protocols* **2014**, *9*, 1944–1955.
- ¹⁶ Arjmandi-Tash, H.; Belyaeva, L. A.; Schneider, G. F. Single molecule detection with graphene and other two-dimensional materials: nanopores and beyond. *Chem. Soc. Rev.* **2016**, *45*, 476–493.
- ¹⁷ Sekhon, S. S.; Kaur, P.; Kim, Y.-H.; Sekhon, S. S. 2D graphene oxide-aptamer conjugate materials for cancer diagnosis. *npj 2D Materials and Applications* **2021**, *5*, 21.
- ¹⁸ Kolesnichenko, P. V.; Zhang, Q.; Zheng, C.; Fuhrer, M. S.; Davis, J. A. Multidimensional analysis of excitonic spectra of monolayers of tungsten disulphide: toward computer-aided identification of structural and environmental perturbations of 2D materials. *Machine Learning: Science and Technology* **2021**, *2*, 025021.
- ¹⁹ Norouzi, M.; Yathindranath, V.; Thliveris, J. A.; Kopec, B. M.; Siahaan, T. J.; Miller, D. W. Doxorubicin-loaded iron oxide nanoparticles for glioblastoma therapy: a combinational approach for enhanced delivery of nanoparticles. *Scientific Reports* **2020**, *10*, 11292.
- ²⁰ Chen, J.; Qian, C.; Ren, P.; Yu, H.; Kong, X.; Huang, C.; Luo, H.; Chen, G. Light-Responsive Micelles Loaded With Doxorubicin for Osteosarcoma Suppression. *Frontiers in Pharmacology* **2021**, *12*, 1378.
- ²¹ Zhong, Y.; Meng, F.; Deng, C.; Mao, X.; Zhong, Z. Targeted inhibition of human hematological cancers in vivo by doxorubicin encapsulated in smart lipoic acid-crosslinked hyaluronic acid nanoparticles. *Drug delivery* **2017**, *24*, 1482–1490.
- ²² He, Y.; Qiu, X. Chidamide combined with doxorubicin leads to synergistic anti-cancer effect and induces autophagy through inhibiting the PI3K/Akt/mTOR pathway in anaplastic thyroid carcinoma. *bioRxiv* **2020**, 2020.05.19.105288.

- ²³ Yuan, Z. et al. Pegylated liposomal doxorubicin in patients with epithelial ovarian cancer. *Journal of Ovarian Research* **2021**, *14*, 12.
- ²⁴ Carvalho, F. S.; Burgeiro, A.; Garcia, R.; Moreno, A. J.; Carvalho, R. A.; Oliveira, P. J. Doxorubicin-Induced Cardiotoxicity: From Bioenergetic Failure and Cell Death to Cardiomyopathy. *Medicinal Research Reviews* **2014**, *34*, 106–135.
- ²⁵ Hofman, J.; Skarka, A.; Havrankova, J.; Wsol, V. Pharmacokinetic interactions of breast cancer chemotherapeutics with human doxorubicin reductases. *Biochemical Pharmacology* **2015**, *96*, 168–178.
- ²⁶ Mitry, M. A.; Edwards, J. G. Doxorubicin induced heart failure: Phenotype and molecular mechanisms. *IJC Heart & Vasculature* **2016**, *10*, 17–24.
- ²⁷ Umsumarng, S.; Pitchakarn, P.; Sastraruji, K.; Yodkeeree, S.; Ung, A. T.; Pyne, S. G.; Limtrakul, P. Reversal of Human Multi-Drug Resistance Leukaemic Cells by Stemofoline Derivatives via Inhibition of P-Glycoprotein Function. *Basic & Clinical Pharmacology & Toxicology* **2015**, *116*, 390–397.
- ²⁸ Sun, X.; Liu, Z.; Welsher, K.; Robinson, J. T.; Goodwin, A.; Zaric, S.; Dai, H. Nano-graphene oxide for cellular imaging and drug delivery. *Nano Research* **2008**, *1*, 203–212.
- ²⁹ Chekin, F.; Myshin, V.; Ye, R.; Melinte, S.; Singh, S. K.; Kurungot, S.; Boukherroub, R.; Szunerits, S. Graphene-modified electrodes for sensing doxorubicin hydrochloride in human plasma. *Analytical and Bioanalytical Chemistry* **2019**, *411*, 1509–1516.
- ³⁰ Hasanzadeh, M.; Hashemzadeh, N.; Shadjou, N.; Eivazi-Ziaei, J.; Khoubnasabjafari, M.; Jouyban, A. Sensing of doxorubicin hydrochloride using graphene quantum dot modified glassy carbon electrode. *Journal of Molecular Liquids* **2016**, *221*, 354–357.
- ³¹ Yang, Z.; Yang, D.; Zeng, K.; Li, D.; Qin, L.; Cai, Y.; Jin, J. Simultaneous Delivery of anti-miR-21 and Doxorubicin by Graphene Oxide for Reducing Toxicity in Cancer Therapy. *ACS Omega* **2020**, *5*, 14437–14443.
- ³² Pei, X.; Zhu, Z.; Gan, Z.; Chen, J.; Zhang, X.; Cheng, X.; Wan, Q.; Wang, J. PEGylated nano-graphene oxide as a nanocarrier for delivering mixed anticancer drugs to improve anticancer activity. *Scientific Reports* **2020**, *10*, 2717.
- ³³ Zong, C.; Xu, M.; Xu, L.-J.; Wei, T.; Ma, X.; Zheng, X.-S.; Hu, R.; Ren, B. Surface-Enhanced Raman Spectroscopy for Bioanalysis: Reliability and Challenges. *Chem. Rev.* **2018**, *118*, 4946–4980.
- ³⁴ Gautier, J.; Munnier, E.; Douziech-Eyrolles, L.; Paillard, A.; Dubois, P.; Chourpa, I. SERS spectroscopic approach to study doxorubicin complexes with Fe²⁺ ions and drug release from SPION-based nanocarriers. *Analyst* **2013**, *138*, 7354–7361.
- ³⁵ Huang, J.; Zong, C.; Shen, H.; Cao, Y.; Ren, B.; Zhang, Z. Tracking the intracellular drug release from graphene oxide using surface-enhanced Raman spectroscopy. *Nanoscale* **2013**, *5*, 10591–8.
- ³⁶ Farhane, Z.; Bonnier, F.; Casey, A.; Byrne, H. J. Raman micro spectroscopy for in vitro drug screening: subcellular localisation and interactions of doxorubicin. *The Analyst* **2015**, *140*, 4212–23.
- ³⁷ Farhane, Z.; Bonnier, F.; Byrne, H. J. Monitoring doxorubicin cellular uptake and trafficking using in vitro Raman microspectroscopy: short and long time exposure effects on lung cancer cell lines. *Analytical and Bioanalytical Chemistry* **2017**, *409*, 1333–1346.
- ³⁸ Littl, L.; Amendola, V.; Toffoli, G.; Meneghetti, M. Detection of low-quantity anticancer drugs by surface-enhanced Raman scattering. *Analytical and Bioanalytical Chemistry* **2016**, *408*, 2123–2131.
- ³⁹ Zhang, K.; Wang, J.; Liu, T.; Luo, Y.; Loh, X. J.; Chen, X. Machine Learning-Reinforced Noninvasive Biosensors for Healthcare. *Adv. Healthcare Mater.* **2021**, 2100734.
- ⁴⁰ Misun, P. M.; Rothe, J.; Schmid, Y. R. F.; Hierlemann, A.; Frey, O. Multi-analyte biosensor interface for real-time monitoring of 3D microtissue spheroids in hanging-drop networks. *Microsystems & Nanoengineering* **2016**, *2*, 16022.
- ⁴¹ Cui, F.; Yue, Y.; Zhang, Y.; Zhang, Z.; Zhou, H. S. Advancing Biosensors with Machine Learning. *ACS Sens.* **2020**, *5*, 3346–3364.
- ⁴² Kalmykov, A.; Huang, C.; Bliley, J.; Shiwarski, D.; Tashman, J.; Abdullah, A.; Rastogi, S. K.; Shukla, S.; Mataev, E.; Feinberg, A. W.; Hsia, K. J.; Cohen-Karni, T. Organ-on-a-chip: Three-dimensional self-rolled biosensor array for electrical interrogations of human electrogenic spheroids. *Sci Adv* **2019**, *5*, eaax0729.
- ⁴³ Novoselov, K. S.; Mishchenko, A.; Carvalho, A.; Castro Neto, A. H. 2D materials and van der Waals heterostructures. *Science* **2016**, *353*, aac9439.
- ⁴⁴ Jeong, S. et al. Fluorescence-Raman Dual Modal Endoscopic System for Multiplexed Molecular Diagnostics. *Scientific Reports* **2015**, *5*, 9455.
- ⁴⁵ Ma, Q.; Ren, G.; Mitchell, A.; Ou, J. Z. Recent advances on hybrid integration of 2D materials on integrated optics platforms. *Nanophotonics* **2020**, *9*, 2191–2214.
- ⁴⁶ AlaguVibisha, G.; Nayak, J. K.; Maheswari, P.; Priyadharsini, N.; Nisha, A.; Jaroszewicz, Z.; Rajesh, K. B.; Jha, R. Sensitivity enhancement of surface plasmon resonance sensor using hybrid configuration of 2D materials over bimetallic layer of Cu-Ni. *Optics Communications* **2020**, *463*, 125337.
- ⁴⁷ Mak, K. F.; He, K.; Lee, C.; Lee, G. H.; Hone, J.; Heinz, T. F.; Shan, J. Tightly bound trions in monolayer MoS₂. *Nature Materials* **2013**, *12*, 207–211.
- ⁴⁸ Mouri, S.; Miyauchi, Y.; Matsuda, K. Tunable Photoluminescence of Monolayer MoS₂ via Chemical Doping. *Nano Lett.* **2013**, *13*, 5944–5948.
- ⁴⁹ Catalan-Gomez, S.; Briones, M.; Cortijo-Campos, S.; Garcia-Mendiola, T.; de Andres, A.; Garg, S.; Kung, P.; Lorenzo, E.; Pau, J. L.; Redondo-Cubero, A. Breast cancer biomarker detection through the photoluminescence of epitaxial monolayer MoS₂ flakes. *Scientific Reports* **2020**, *10*, 16039.
- ⁵⁰ Aryeetey, F.; Pourianejad, S.; Ayanbajo, O.; Nowlin, K.; Ignatova, T.; Aravamudhan, S. Bandgap recovery of monolayer MoS₂ using defect engineering and chemical doping. *RSC Adv.* **2021**, *11*, 20893–20898.
- ⁵¹ Barja, S. et al. Identifying substitutional oxygen as a prolific point defect in monolayer transition metal dichalcogenides.

- Nature Communications* **2019**, *10*, 3382.
- ⁵² Mitterreiter, E. et al. The role of chalcogen vacancies for atomic defect emission in MoS₂. *Nature Communications* **2021**, *12*, 3822.
- ⁵³ Schuler, B.; Cochrane, K. A.; Kastl, C.; Barnard, E. S.; Wong, E.; Borys, N. J.; Schwartzberg, A. M.; Ogletree, D. F.; de Abajo, F. J. G.; Weber-Bargioni, A. Electrically driven photon emission from individual atomic defects in monolayer WS₂. *Sci Adv* **2020**, *6*, eabb5988.
- ⁵⁴ Thiruraman, J. P.; Fujisawa, K.; Danda, G.; Das, P. M.; Zhang, T.; Bolotsky, A.; Perea-Lopez, N.; Nicolai, A.; Senet, P.; Terrones, M.; Drndic, M. Angstrom-Size Defect Creation and Ionic Transport through Pores in Single-Layer MoS₂. *Nano Lett.* **2018**, *18*, 1651–1659.
- ⁵⁵ Komsa, H.-P.; Krashennnikov, A. V. Native defects in bulk and monolayer MoS₂ from first principles. *Phys. Rev. B* **2015**, *91*, 125304.
- ⁵⁶ Zheng, X. et al. Spatial defects nanoengineering for bipolar conductivity in MoS₂. *Nature Communications* **2020**, *11*, 3463.
- ⁵⁷ Nan, H.; Wang, Z.; Wang, W.; Liang, Z.; Lu, Y.; Chen, Q.; He, D.; Tan, P.; Miao, F.; Wang, X.; Wang, J.; Ni, Z. Strong Photoluminescence Enhancement of MoS₂ through Defect Engineering and Oxygen Bonding. *ACS Nano* **2014**, *8*, 5738–5745.
- ⁵⁸ Rao, R.; Islam, A. E.; Singh, S.; Berry, R.; Kawakami, R. K.; Maruyama, B.; Katoch, J. Spectroscopic evaluation of charge-transfer doping and strain in graphene/MoS₂ heterostructures. *Phys. Rev. B* **2019**, *99*, 195401.
- ⁵⁹ Neumann, C.; Reichardt, S.; Venezuela, P.; Droegeler, M.; Banszerus, L.; Schmitz, M.; Watanabe, K.; Taniguchi, T.; Mauri, F.; Beschoten, B.; Rotkin, S. V.; Stampfer, C. Raman spectroscopy as probe of nanometre-scale strain variations in graphene. *Nature Communications* **2015**, *6*, 8429.
- ⁶⁰ Mueller, N. S. et al. Evaluating arbitrary strain configurations and doping in graphene with Raman spectroscopy. *2D Materials* **2017**, *5*, 015016.
- ⁶¹ Narula, R.; Bonini, N.; Marzari, N.; Reich, S. Dominant phonon wave vectors and strain-induced splitting of the 2D Raman mode of graphene. *Phys. Rev. B* **2012**, *85*, 115451.
- ⁶² Leong, W. S.; Wang, H.; Yeo, J.; Martin-Martinez, F. J.; Zubair, A.; Shen, P.-C.; Mao, Y.; Palacios, T.; Buehler, M. J.; Hong, J.-Y.; Kong, J. Paraffin-enabled graphene transfer. *Nature Communications* **2019**, *10*, 867.
- ⁶³ Bousige, C.; Balima, F.; Machon, D.; Pinheiro, G. S.; Torres-Dias, A.; Nicolle, J.; Kalita, D.; Bendiab, N.; Marty, L.; Bouchiat, V.; Montagnac, G.; Souza Filho, A. G.; Poncharal, P.; San-Miguel, A. Biaxial Strain Transfer in Supported Graphene. *Nano Lett.* **2017**, *17*, 21–27.
- ⁶⁴ Banszerus, L.; Janssen, H.; Otto, M.; Epping, A.; Taniguchi, T.; Watanabe, K.; Beschoten, B.; Neumaier, D.; Stampfer, C. Identifying suitable substrates for high-quality graphene-based heterostructures. *2D Materials* **2017**, *4*, 025030.
- ⁶⁵ Seo, Y.-M.; Jang, W.; Gu, T.; Seok, H.-J.; Han, S.; Choi, B. L.; Kim, H.-K.; Chae, H.; Kang, J.; Whang, D. Defect-Free Mechanical Graphene Transfer Using n-Doping Adhesive Gel Buffer. *ACS Nano* **2021**,
- ⁶⁶ Gao, L.; Ren, W.; Xu, H.; Jin, L.; Wang, Z.; Ma, T.; Ma, L.-P.; Zhang, Z.; Fu, Q.; Peng, L.-M.; Bao, X.; Cheng, H.-M. Repeated growth and bubbling transfer of graphene with millimetre-size single-crystal grains using platinum. *Nature Communications* **2012**, *3*, 699–.
- ⁶⁷ Zhang, Z.-M.; Chen, S.; Liang, Y.-Z. Baseline correction using adaptive iteratively reweighted penalized least squares. *Analyst* **2010**, *135*, 1138–1146.
- ⁶⁸ Lee, J. E.; Ahn, G.; Shim, J.; Lee, Y. S.; Ryu, S. Optical separation of mechanical strain from charge doping in graphene. *Nature Communications* **2012**, *3*, 1024.
- ⁶⁹ Das, A.; Chakraborty, B.; Piscanec, S.; Pisana, S.; Sood, A. K.; Ferrari, A. C. Phonon renormalization in doped bilayer graphene. *Phys. Rev. B* **2009**, *79*, 155417.
- ⁷⁰ Chakraborty, B.; Bera, A.; Muthu, D. V. S.; Bhowmick, S.; Waghmare, U. V.; Sood, A. K. Symmetry-dependent phonon renormalization in monolayer MoS₂ transistor. *Phys. Rev. B* **2012**, *85*, 161403.
- ⁷¹ Larentis, S.; Tolsma, J. R.; Fallahazad, B.; Dillen, D. C.; Kim, K.; MacDonald, A. H.; Tutuc, E. Band Offset and Negative Compressibility in Graphene-MoS₂ Heterostructures. *Nano Letters* **2014**, *14*, 2039–2045, PMID: 24611616.
- ⁷² Peelaers, H.; Van de Walle, C. G. Effects of strain on band structure and effective masses in MoS₂. *Phys. Rev. B* **2012**, *86*, 241401.
- ⁷³ Yu, Y.-J.; Zhao, Y.; Ryu, S.; Brus, L. E.; Kim, K. S.; Kim, P. Tuning the Graphene Work Function by Electric Field Effect. *Nano Letters* **2009**, *9*, 3430–3434, PMID: 19719145.
- ⁷⁴ Knox, K. R.; Wang, S.; Morgante, A.; Cvetko, D.; Locatelli, A.; Menten, T. O.; Niño, M. A.; Kim, P.; Osgood, R. M. Spectromicroscopy of single and multilayer graphene supported by a weakly interacting substrate. *Phys. Rev. B* **2008**, *78*, 201408.